Hydrothermal minerals and microstructures in the Silangkitang geothermal field along the Great Sumatran fault zone, Sumatra, Indonesia

D.E. Moore*
S. Hickman
D.A. Lockner
U.S. Geological Survey, Menlo Park, California 94025, USA

P.F. Dobson[†]
Unocal Geothermal and Power Operations, Santa Rosa, California 95401, USA

ABSTRACT

Detailed study of core samples of silicic tuff recovered from three geothermal wells along the strike-slip Great Sumatran fault zone near Silangkitang, North Sumatra, supports a model for enhanced hydrothermal circulation adjacent to this major plate-boundary fault. Two wells (A and C) were drilled nearly vertically ~1 km southwest of the eastern (i.e., the principal) fault trace, and the third, directional well (B) was drilled eastward from the site of well A to within ~100 m of the principal fault trace. The examined core samples come from depths of 1650–2120 m at measured well temperatures of 180–320 °C. The samples collected near the principal fault trace have the highest temperatures, the largest amount of secondary pore space that correlates with high secondary permeability, and the most extensive hydrothermal mineral development. Secondary permeability and the degree of hydrothermal alteration decrease toward the southwestern margin of the fault zone. These features indicate episodic, localized flow of hot, possibly CO_2-rich fluids within the fault zone. The microstructure populations identified in the core samples correlate to the subsidiary fault patterns typical of strike-slip faults. The geothermal reservoir appears to be centered on the fault zone, with the principal fault strands and adjoining, highly fractured and hydrothermally altered rock serving as the main conduits for vertical fluid flow and advective heat transport from deeper magmatic sources.

Keywords: hydrothermal conditions, Indonesia, mineral assemblages, strike-slip faults, Sumatra.

INTRODUCTION

The Great Sumatran fault zone is an active, northwest-trending, right-lateral strike-slip fault that accommodates the arc-parallel component of oblique subduction at the Java Trench (Fig. 1). The fault is close to the axis of the magmatic arc on Sumatra, and the concentration of features such as hot and warm springs, fumaroles, and altered rock in the vicinity of the fault zone suggests its potential as an important source of geothermal energy (Hochstein and Sudarman, 1993). In 1993, Unocal entered into a contract with Pertamina and PLN, the Indonesian state-owned oil and power companies, respectively, for exploration and development of geothermal energy in the Sarulla area of North Sumatra (Gunderson et al., 1995, 2000). Unocal subsequently afforded the U.S. Geological Survey the opportunity to examine petrographically 13 core samples recovered from three exploratory geothermal wells.

Much recent emphasis has been placed on the possible role of fluids in the earthquake cycle and conversely the role of fault zones in focusing fluid flow in the crust (Hickman et al., 1995, and references therein). Many of the observations used to model the hydrologic properties and mechanical behavior of fault zones at depth are derived from exhumed faults (e.g., Chester et al., 1993; Evans et al., 1997; Schulz and Evans, 1998) whose mineral assemblages, microstructures, and physical properties may have been modified since the time of active faulting. Unocal's Silangkitang core samples, although few, afford us a unique glimpse of an active strike-slip, plate-boundary fault zone and its environs at depth. The specific objectives of this study are to (1) characterize the distribution and nature of hydrothermal alteration assemblages and identify the controls on their formation within the fault-zone setting, (2) describe the microstructures and determine their relationship to fault-zone geometry and the faulting regime, and (3) examine the interrelationships between fluid-flow and faulting processes at this locality. This information is important for a better understanding of geochemical and tectonic controls on the nature and extent of fault-related geothermal resources, the role of fluids in controlling faulting and earthquake recurrence, and the role of faults as either barriers or conduits to oil and gas migration.

Geologic Background

The island of Sumatra (Fig. 1) is situated along the southwest margin of the Sundaland cratonic block, and it may have formed part of a convergent plate margin since Permian time (McCourt et al., 1996). Older belts of subduction-related plutonic rocks on Sumatra all have a roughly northwest trend subparallel to the present magmatic arc, suggesting that the configuration of this part of the subduction

*E-mail: dmoore@usgs.gov.
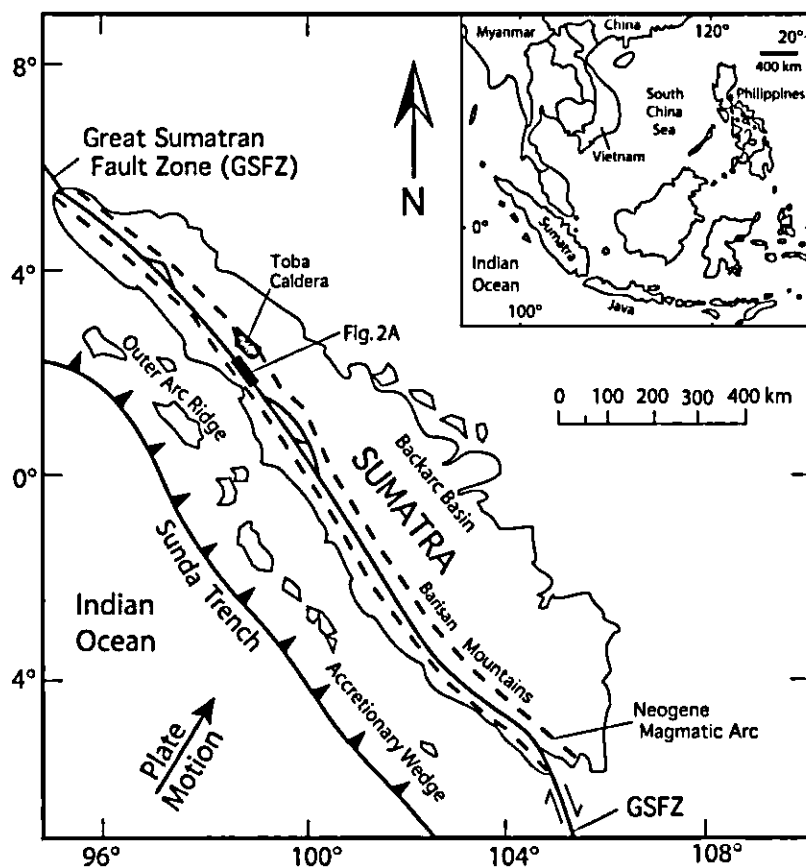[†]Present address: Lawrence Berkeley National Laboratory, Berkeley, California 94720, USA.

Figure 1. Tectonic setting of Sumatra in southeast Asia. The Great Sumatran fault zone (GSFZ) is associated with the active magmatic arc on the island (map modified from Hamilton, 1979).

(e.g., Katili, 1970; Simandjuntak and Barber, 1996) have formed at these extensional segment boundaries, and volcanic edifices are situated within some of them (Bellier and Sébrier, 1994; Sieh and Natawidjaja, 2000).

The Sarulla contract area in North Sumatra is centered over the Great Sumatran fault zone, which here consists of two strands: the well-defined eastern strand, which forms the principal trace, and a less distinct western strand located 4–6 km southwest of the eastern trace (Gunderson et al., 2000). In the central part of the contract area the principal strand forms the northeast boundary of the Sarulla graben (Fig. 2A, from Gunderson et al., 1995). Here, the principal strand brings a Paleozoic metasedimentary sequence—including quartzite, phyllite, and limestone (Aspden et al., 1982)—on the northeast side into fault contact with the Quaternary volcanic sequence that fills the graben. The arc volcanic rocks range in age from 0.1 to 1.8 Ma (Gunderson et al., 1995), and they include lava flows and breccias and rhyolite to basaltic andesite ash-flow and ash-fall tuffs. A roughly 1-km-wide zone of subsidiary faulting subparallel to the Great Sumatran fault zone extends southwest from the principal strand within the Sarulla graben (Fig. 2B). The southwest boundary of the graben corresponds to the western strand of the fault zone (Fig. 2B), but the fault trace is poorly defined and was not included in the geologic map.

One focus of geothermal exploration by Unocal in the Sarulla contract area has been centered around a group of active thermal features around the Great Sumatran fault zone near Silangkitang, at the northern end of the Sarulla graben, associated with a Quaternary eruptive center (Gunderson et al., 1995). Fluids discharged at the surface in this area (Hochstein and Sudarman, 1993; Gunderson et al., 1995) are dilute, nearly pH neutral, Cl-rich waters with a low Ca content. The temperatures of 260–270 °C for some of these waters, determined by cation geothermometers, indicate that the waters rose rapidly from a high-temperature reservoir (Gunderson et al., 1995).

Core Samples and Scope of Study

We examined 13 core samples, each 6.3 cm in diameter and 14–60 cm long, from three wells. Boreholes A and C are situated ~1 km west of the principal strand of the Great Sumatran fault zone, close to the southwest limit of the zone of subsidiary faulting associated with that strand; well C is ~1.2 km northwest of well A (Fig. 2B). Well C is sited southwest

system has remained almost the same throughout its history. The present period of subduction followed a middle Oligocene collision event; plutonic activity became important in the early Miocene, and volcanism spanned the arc by the middle Miocene (McCourt et al., 1996). Andesitic volcanism became intense in the Pliocene, and voluminous rhyolitic volcanism commenced during Pliocene-Pleistocene time (Hochstein and Sudarman, 1993).

The current subduction regime involves northeast motion of the Indian Ocean plate (Fig. 1) at ~7.5 cm/yr (McCaffrey, 1996). Subduction of the Investigator Fracture Zone coincides with the location of the Toba caldera (Fig. 1) and with an apparent offset in the volcanic chain along the arc trend (Fauzi et al., 1996). Subduction beneath Sumatra is oblique at ~50°–65° (Simandjuntak and Barber, 1996), and the plate motion is roughly partitioned into a component of convergence perpendicular to the trench and a component of right-lateral strike-slip faulting on the Great Sumatran fault zone parallel to the trench (Fitch, 1972). Sieh and Natawidjaja (2000)

suggested that the fault zone formed at ca. 2 Ma and that the maximum displacement along it is ~23 km. The slip rate on the fault zone obtained from offset geomorphic features increases from ~6 ± 4 mm/yr in the south to ~23 ± 2 mm/yr near the Toba caldera (Sieh et al., 1994; Bellier and Sébrier, 1995). Although the strongest earthquakes felt on Sumatra are associated with the subducting plate (Newcomb and McCann, 1987), the Great Sumatran fault zone has generated historical earthquakes with magnitudes as great as 7.5 (Fitch, 1972; Sieh et al., 1994). Mount and Suppe (1992) determined that the maximum regional horizontal stress makes a 70°–80° angle to the strike of the fault, which implies that a low shear stress is acting on the fault. Thus, the fault zone appears to be much weaker than the surrounding crust, as is also the case for the San Andreas fault in California (Mount and Suppe, 1987; Zoback et al., 1987; Hickman, 1991). The fault zone is highly segmented, and most of the principal segment boundaries are dilational in nature (Sieh and Natawidjaja, 1998, 2000). A series of grabens
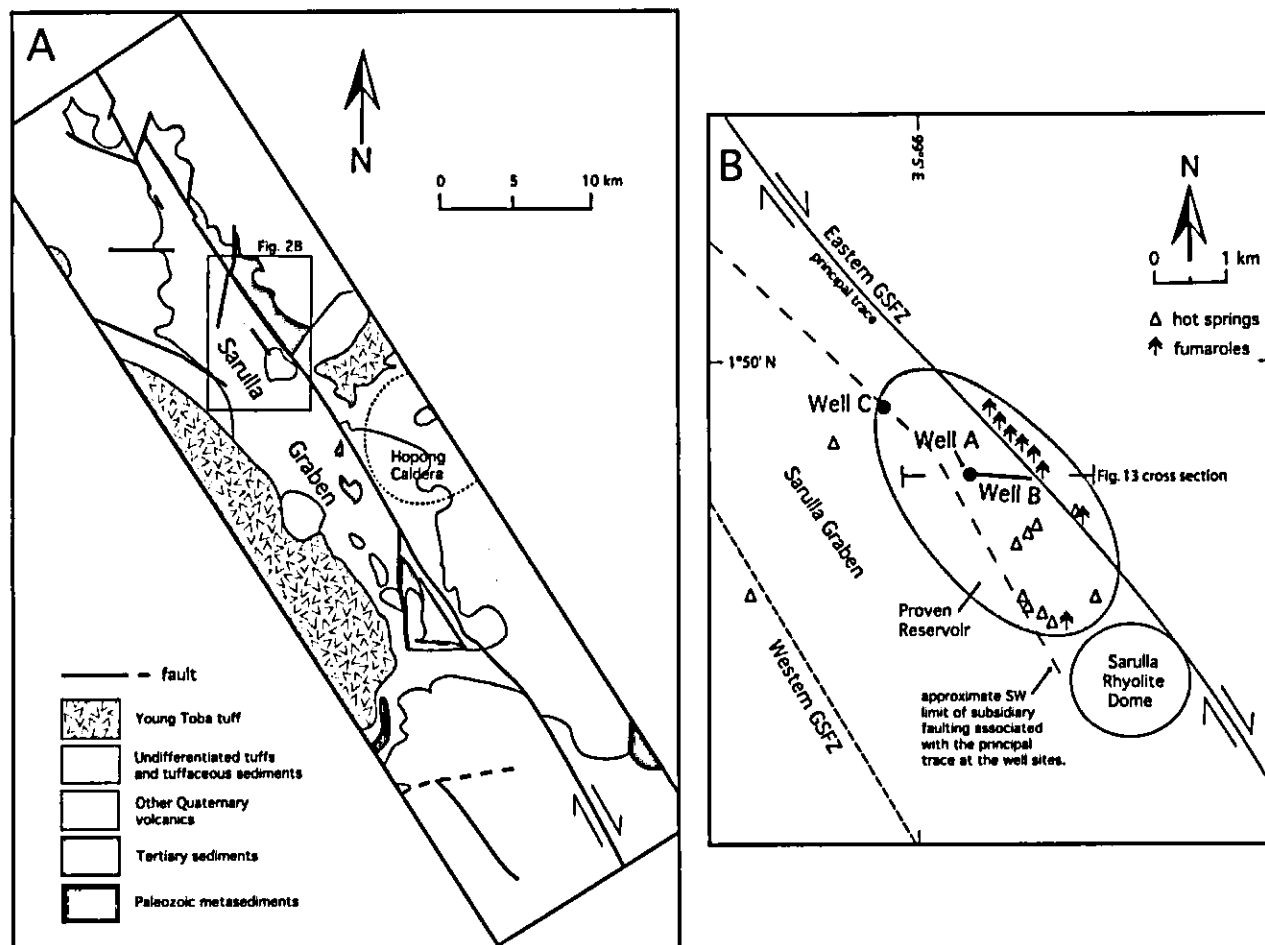
Figure 2. (A) Generalized geologic map of the Unocal contract area (modified from Gunderson et al., 1995). The southwest boundary of the Sarulla graben, marked by the western strand of the Great Sumatran fault zone, is indistinct, and the fault trace was not included in this map. (B) Schematic locality map of the three wells investigated in this study (modified from Gunderson et al., 2000; the well names used by Gunderson et al. are SIL1-1 for well A, SIL1-2 for well B, and SIL2-1 for well C). Wells A and C were drilled nearly vertically, and they are represented by the filled circles. Well B was drilled at 25°–33° off vertical from the position of well A toward the principal strand of the fault in the direction S84°E, indicated by the heavy line. The well sites are ~500 m above sea level (see cross section in Fig. 13).

of a minor fault trace that dips steeply to the northeast, and well A is ~300 m from another mapped surface trace. These two wells were drilled nearly vertically, with maximum deviations from the vertical of 2.5° and 10° for wells A and C, respectively. Initial drilling of well B was also vertical and located at the site of well A, but the deeper part was deviated 25°–33° in the direction S84°E (Fig. 2B). The deviated part of well B may cross more than one fault strand. The depths at which the examined core samples were collected are presented in Figure 3. The shallowest well B sample (B-1) was collected ~40 m east of a subsidiary fault strand, and the deepest one (B-8) is estimated to have been positioned <100 m from the principal trace. Measured temperatures at the sampled depths are 300–

320 °C for well B, 270–290 °C for well A, and 180–200 °C for well C, which also provided the deepest sample examined (Fig. 3).

One to three polished thin sections were prepared from each piece of core, with the plane of each thin section oriented perpendicular to the axis of the core sample. At least one thin section from each core sample was examined with a scanning electron microscope (SEM) equipped with a high-resolution back-scattered-electron (BSE) detector and an energy-dispersive X-ray (EDX) spectrometer, the latter for qualitative determinations of element abundances. Mineral compositions were obtained from selected thin sections with an automated, five-channel JEOL model 8900L electron microprobe, at operating conditions of 15 kV accelerating voltage, 25 nA beam

current, and beam diameters of 10 to 15 μm. Natural and synthetic minerals were used both for initial standardization and as internal standards during analysis.

MINERAL ASSEMBLAGES AND TEXTURES

Igneous Assemblages

Six of the thirteen core samples (the well A and well C samples, along with sample B-8; Fig. 3) are phenocryst-rich rhyolite tuffs. They contain embayed, rounded quartz crystals up to 5 mm in diameter, subhedral to euhedral plagioclase phenocrysts as long as 3 mm, and somewhat smaller and less numerous, subhedral K-feldspar phenocrysts. The K-feldspar
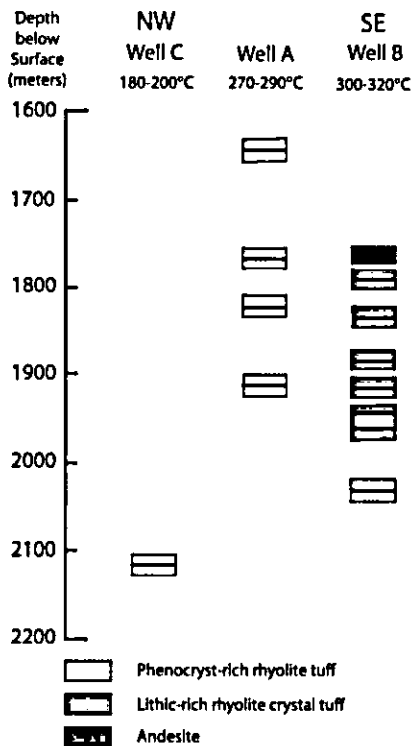
Figure 3. Vertical depths and measured well-bore temperatures for the core samples examined in this study. The heavy horizontal lines mark the sample depths, and the patterned boxes sandwiching the lines indicate the rock type.
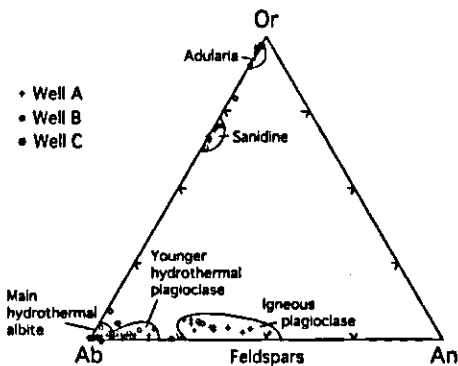

Figure 4. Igneous and hydrothermal feldspar compositions for the core samples studied (Moore, 1997). Most of the hydrothermal mineral compositions are close to the albite (Ab) and orthoclase (Or) end members (An is the anorthite end member), but some of the younger hydrothermal plagioclase crystals are slightly more calcic than the older ones.

TABLE 1. HYDROTHERMAL MINERAL ASSEMBLAGES

Sample number	Well A				Well B								Well C
	A-1	A-2	A-3	A-4	B-1	B-2	B-3	B-4	B-5	B-6	B-7	B-8	C-1
Depth (m)	1644	1769	1825	1911	1763	1791	1835	1885	1912	1942	1961	2031	2116
Quartz	X	X	X	X	X	x	X	X	X	X	X	X	X
Calcite	X	X	X	X	X	X	X	X	X	X	X	X	X
Albite	X	X	X	X	X	X	X	X	X	X	X	X	X
Adularia	X	x	x	x	x	X	X	X	X	X	X	X	X
Epidote						x	x	x	x	x	x	x	
Allanite	x	x	Tr	x	x	x	x	x	x	x	x	x	x
Titanite	X	X	X	X	X	X	X	X	X	X	X	X	x
K-Mica	X	X	X	X	X	X	x	x	x	x	x	x	X
Chlorite	X	X	x	X	X	X	X	X	X	X	X	X	Tr
TiO₂*	X	Tr		x	Tr		x			Tr	x		X
Iron oxide†	Tr	X	X	X	x		x		x		x		
Anhydrite					X	x	X	X	X	X	X	X	
Apatite	x	x	x	x	Tr	x	x	x	x	x	x	x	x
Pyrite		Tr			X	X	X	X	X	X	X	X	X
Sphalerite												Tr	Tr
Galena	Tr		Tr				Tr			Tr	Tr	Tr	Tr
Ilmenite		x	x										
Zircon		Tr	x			x				x	x		Tr

Notes: X—relatively abundant; x—minor; Tr—only one or two crystals found.
*Anatase or rutile.
†Magnetite or hematite (see text).

phenocrysts are Na-rich sanidines, and the plagioclase phenocrysts typically are oligoclase (An₂₆₋₃₀) in composition, but the cores of some plagioclase crystals are as calcic as An₅₀ (Fig. 4; the mineral compositions plotted in this paper are reported and discussed by Moore, 1997). Mafic phenocrysts have all been pseudomorphically replaced by hydrothermal minerals, but on the basis of their crystal outlines they consisted principally of biotite, with a small number of amphiboles. The devitrified groundmass of these six samples has a dusty, mottled appearance and rare spherulitic texture. Well-defined shards are not common; those present are largely undeformed, although locally they are molded around phenocrysts. Samples A-2, A-3, and C-1 contain few lithic fragments, whereas A-4 and B-8 are rich in volcanic lithic fragments that range from rhyolite to andesite in composition. A-4 and B-8 also contain clasts of metasedimentary rock (metashale, metasandstone, and quartzite).

The other well B samples (except B-1; Fig. 3) are lithic-rich rhyolite crystal tuffs whose phenocrysts, all <1 mm long, consist principally of oligoclase along with some quartz and sanidine but no biotite. The groundmass of this group of samples is rich in largely undeformed shards, coarsely crystallized to quartz ± feldspar assemblages, that are embedded in a dark matrix of fine ash. Among the lithic fragments, volcanic rock types predominate, ranging from andesites to crystal-rich rhyolite tuffs that are similar to the well A and well C samples. Numerous fragments of metasedimentary rock and a few plutonic igneous

clasts are also present. The most mafic sample, B-1, is a porphyritic andesite, with plagioclase phenocrysts set in a felted groundmass rich in plagioclase laths.

Hydrothermal Assemblages and Microstructures

Table 1 summarizes the hydrothermal alteration assemblages observed in the wells. Many of these minerals line or fill fractures, some replace phenocrysts of feldspar or mafic minerals, and still others occur in altered groundmass. The character of the alteration and the deformation-related textures and microstructures all vary from well to well. Each well is considered separately below, moving from lower (well C) to higher (well B) measured well temperatures and increasing proximity to the principal trace of the Great Sumatran fault zone.

Well C

The core sample from this well contains a few partly filled dilational fractures (Fig. 5A) and some narrow fractures with small (<0.75 mm) offsets, but little evidence of brittle grain-size reduction or fragmentation accompanying shear. The predominant fracture-filling minerals are quartz and calcite, and the larger quartz-bearing fractures also contain K-mica, pyrite, apatite, TiO₂, albite, K-feldspar, titanite, allanite, and sphalerite. One wide, partly filled fracture is spanned by quartz crystals that grew as crystallographically contiguous overgrowths on quartz phenocrysts that had been broken and separated along the frac-
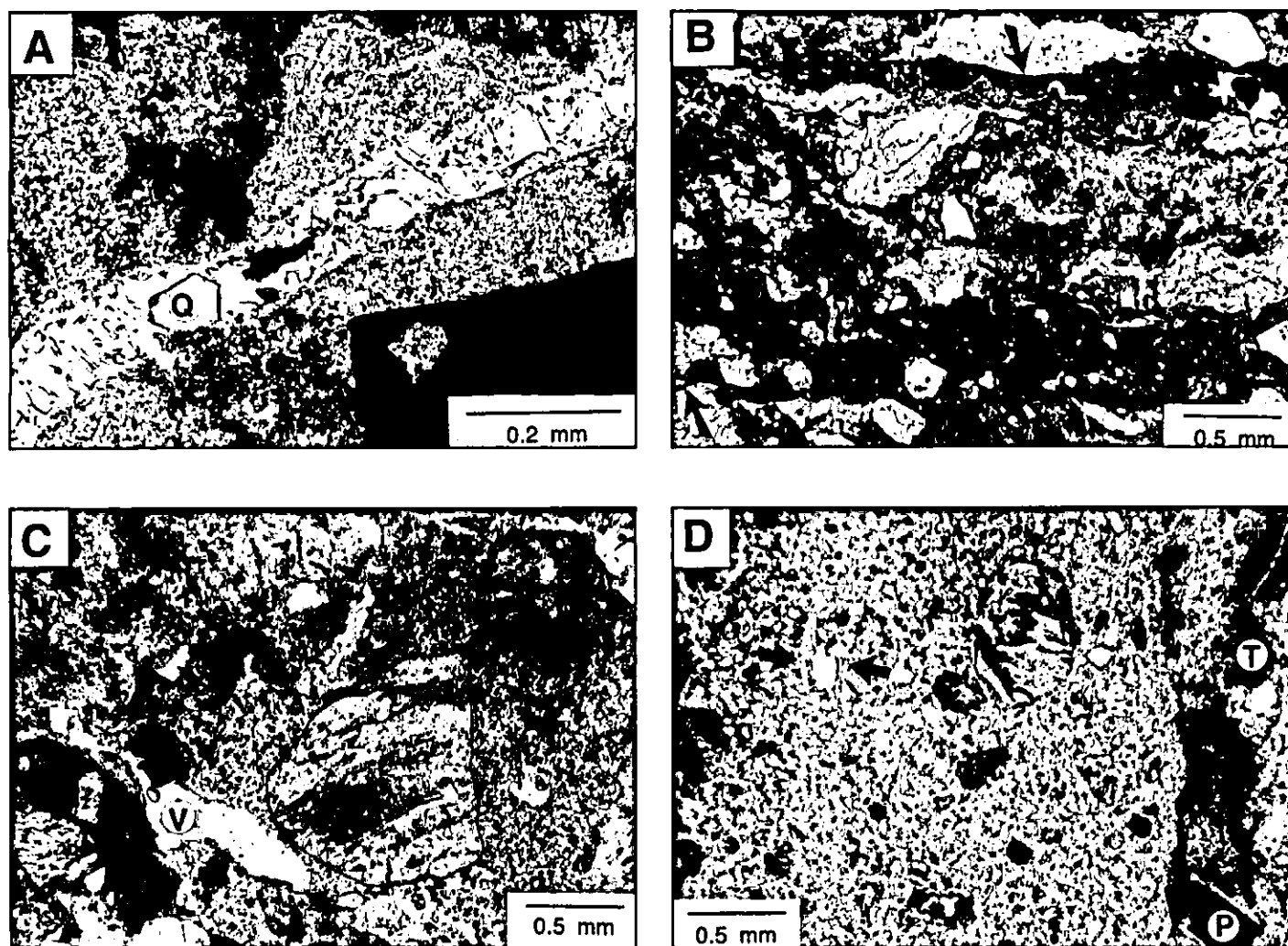
Figure 5. Microstructures. All views are in plane-polarized light. (A) A 150-μm-wide dilational fracture in C-1, traversed by rods of quartz and one larger, euhedral quartz (Q) crystal. (B) Sheared band in A-3 containing variably crushed phenocrysts. The sides, indicated by arrows, are marked by dark hematite deposits, and hematite and calcite fill cracks and voids within the shear. (C) Brecciated sample B-3. A fragment of tuff is in the lower left corner; outlined near the center is a fragment of banded, older cement embedded in slightly coarser-grained cement with the same mineral assemblage. Between these two fragments, a rectangular pyrite crystal is growing into an elongate void (V) space. (D) Right side of a 10-mm-wide band in B-4 that is interpreted to be a heavily recrystallized version of the well A shear seen in Figure 5B. The sides of this shear are marked by concentrations of pyrite (P) and titanite (T). A slightly lighter band (sides indicated by arrows) may be a recent path of fluid flow within the shear; the white area between the arrows is a void.

ture. The overgrowths have a crack-seal texture (Ramsay, 1980) characterized by bands of inclusions aligned parallel to the fracture surface. This texture suggests that the fracture was gradually propped open by repeated episodes of fracturing and healing of the quartz crystals. Smaller euhedral crystals of quartz, pyrite, and other minerals have grown into the open fracture from the walls. Some calcite is associated with the quartz-lined fractures, but more commonly the calcite occurs separately. A TiO_2 mineral borders several of the calcite-filled fractures (Fig. 6A); the larger crystals are reddish brown with a blocky habit, suggestive of either rutile or anatase.

All feldspar phenocrysts in the well C core sample have been altered by hydrothermal fluids, the plagioclase phenocrysts to albite and the sanidine to low-Na K-feldspar + K-mica + albite (Fig. 4). Well-crystallized K-mica is the major replacement mineral of biotite phenocrysts, generally in association with the TiO_2 mineral. The occurrence of chlorite is limited to a few small, rounded patches of pale-green crystals in altered plagioclase phenocrysts. Euhedral igneous magnetite crystals have a corroded appearance, and no hydrothermal iron oxides have crystallized. However, pyrite crystals up to 0.75 mm on a side are scattered throughout the tuff, some of

them mantling the corroded magnetite crystals and others straddling narrow fractures. Probable effects of hydrothermal fluids on the groundmass of the tuff include the blurring of shard outlines and the localized coarsening of the K-mica + albite + quartz + K-feldspar assemblage.

Well A

In contrast to well C, well A is characterized by the prominence of hematite and the near absence of pyrite, the common occurrence of chlorite and titanite, and the prevalence of small-scale sheared zones over large-scale open fractures. In particular, no wide
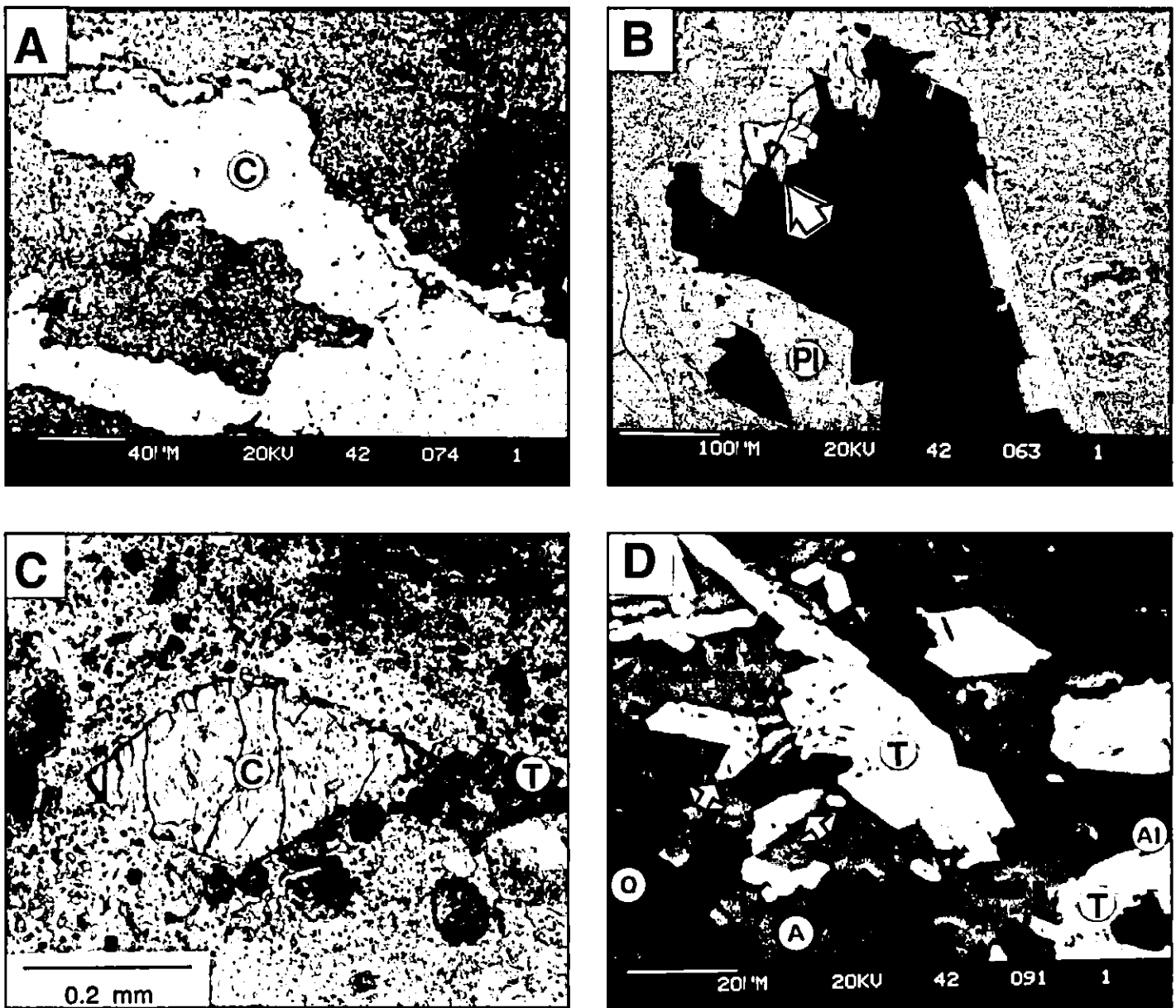
Figure 6. Mineral textures. (A) Backscattered-electron (BSE) SEM image of a calcite (C) vein in C-1, with a partial border of bright TiO_2 crystals. (B) BSE image of a cavity (black) that takes up most of a small plagioclase (Pl) phenocryst in A-1. The remnants of plagioclase have euhedral outlines adjacent to the cavity, and they are albitized to An_{4-8}; some tiny, possibly younger, rods of plagioclase extend from the plagioclase surface. At the top of the cavity, the bright titanite crystal is intergrown with a small oligoclase crystal, indicated by the arrow, that may also be new growth. (C) Photomicrograph of a calcite (C) crystal in a multiply sheared zone in B-8. The margins of the crystal and internal fractures have a dark, corroded appearance, and the upper two sides are embayed by adularia, quartz, and chlorite crystals. A line of darker titanite (T) crystals follows the lower right side. Plane-polarized light. (D) BSE image showing relationships among titanite, allanite, and epidote in an adularia-rich (A) vein in B-6. Blades of bright allanite extend from the margins of larger titanite (T) crystals. Small epidote crystals, indicated by arrows, occur as rims on the allanite and as small lozenge-shaped crystals growing out from the margins of the allanite. Darker grains dispersed in the adularia are quartz (Q) and albite (Al).

extensional fractures lined with euhedral crystals were found in the well A samples; instead, they contain shear bands up to 5 mm wide that consist of fractured to finely granulated phenocrysts and groundmass (Fig. 5B). In general, the narrower the shear band, the more

highly comminuted the tuff is within it. The shears are not heavily overprinted by recrystallization or alteration, and even very small fragments of sanidine and plagioclase retain their primary compositions. However, the boundaries of the wider shears typically are

marked by deposits of hematite (Fig. 5B), and calcite and hematite line some of the cracks and void spaces within the shears. Although calcite and hematite are the most important fracture-filling minerals in well A, several of these small-scale veins consist of calcite +

chlorite + titanite. The well A samples contain almost no sulfur-bearing minerals, but a few late-formed, minute crystals of pyrite and other S-bearing phases were encountered both in the pore spaces of a hematite-lined shear in A-2 and in fresh cracks extending away from that shear.

Many of the phenocrysts of plagioclase and K-feldspar in A-1 are riddled with cavities, with one or two small crystals of titanite, allanite, calcite, or quartz around the edges (Fig. 6B). The remnants of plagioclase and K-feldspar surrounding the voids have euhedral terminations (Fig. 6B) whose compositions typically are albite (An_{4-8}) and Na-poor K-feldspar, respectively (Fig. 4). One exception is the small crystal of oligoclase (An_{16}), shown in Figure 6B, that is intergrown with titanite along a void in an albitized plagioclase. The proportion of feldspar phenocrysts containing cavities decreases progressively with increasing depth in the well, and the individual voids tend to be smaller. Instead, the deeper-level feldspars show patchy replacement by calcite and alteration along fractures.

A TiO_2 mineral—rutile or anatase—is associated with calcite veins; in A-1 and A-4, reddish, blocky TiO_2 crystals in feldspar phenocrysts are rimmed by titanite. The few amphibole phenocrysts in these tuff samples have been replaced principally by calcite, with associated K-mica, titanium-iron oxides, and minor amounts of quartz. In some crystals, narrow bands of K-mica and opaque minerals outline the former amphibole cleavage planes. The replacement of biotite phenocrysts varies between two end members: K-mica + TiO_2 (or ilmenite) and chlorite + titanite, with accessory quartz, K-feldspar, and calcite in both occurrences. The K-mica end member was found only in A-1 and A-2, and the chlorite end member was found only in A-4. Where all four alteration minerals appear in the same biotite crystal, the textures suggest that the chlorite + titanite assemblage replaces K-mica + titanium oxide.

Well B

The mineralization and textures of well B are distinctive in several respects, among them the large number of wide, only partly filled fractures, the presence of brecciated zones (Fig. 5C), and the extensive hydrothermal deposits dominated by adularia but also including anhydrite and rare epidote. Calcite and quartz are the principal fracture- and cavity-filling minerals in the two shallowest samples, but adularia is most abundant at greater depths. Some calcite veins in the deeper well B core samples are crosscut by adularia-rich

veins, and in a repeatedly altered zone in B-8, the edges of some calcite crystals are partly rimmed by titanite and embayed by small crystals of adularia, quartz, and chlorite (Fig. 6C). In that same zone, localized new growth of calcite was also observed, in some cases within millimeters of partly replaced calcite crystals. Adularia principally occurs as fine-grained anhedral masses that fill narrow fractures or replace the groundmass of the tuffs in combination with quartz, chlorite, albite, apatite, and titanite. In addition, adularia forms overgrowths on both plagioclase and K-feldspar phenocrysts, and medium- to coarse-grained euhedral crystals of adularia line the wider, open fractures. Some of the open fractures are also traversed by anhydrite crystals. Textures suggest alternating growth of adularia and anhydrite.

Only well B contains high-porosity brecciated zones. Most notably, the entire 14-cm-long B-3 core sample is an agglomeration of tuff fragments as long as 3.5 cm that are cemented together by adularia-rich hydrothermal deposits (Fig. 5C). The hydrothermal cement is itself brecciated; for example, Figure 5C shows pieces of microcrystalline cement with a modest fabric embedded in a slightly coarser grained cement of the same minerals. One B-3 thin section contains ~50% tuff, 30% cement, and 20% pore space, indicating that the volume of this brecciated zone has approximately doubled. Samples B-7 and B-8 have more restricted brecciated zones with tuff fragments ≤ 1 cm long. These latter zones have well-defined planar boundaries, but they widen locally where they intersect other fractures. Euhedral anhydrite crystals as long as 2 cm cross the pore spaces of the breccias. B-4 has an incipient brecciated zone, 2.5 to 5 mm wide, that formed along one side of an older, calcite-filled fracture. The rock adjoining this zone on the other side contains numerous fractures up to 0.5 mm wide that are partly filled with hydrothermal minerals. These fractures have a variety of orientations, but phenocrysts broken and separated by them all indicate the same opening direction, roughly perpendicular to the strike of the brecciated zone.

A number of prominent bands as wide as ~10 mm consist of a matrix of fine-grained adularia + quartz + chlorite + anhydrite + titanite + pyrite + apatite and a scattering of relatively small, partly altered igneous phenocrysts and lithic fragments (Fig. 5D). The edges of the bands are marked by pyrite + titanite + allanite ± epidote. These fine-grained bands are interpreted to represent more highly recrystallized and cemented versions of the shear bands common in well A

(Fig. 5B); the pyrite-rich margins are the equivalent of the hematite-lined margins of the well A shears. The relatively small size of the feldspar phenocrysts in the bands suggests that these feldspars are the remnants of fragmented crystals.

Many plagioclase phenocrysts in well B, particularly those caught up in the breccias and shears (Fig. 5, C and D), have been thoroughly albitized to approximately An_2. In turn, several of these albitized crystals have overgrowths of albite with composition An_{7-10} (Fig. 4). In B-7, for example, an albitized (An_2) phenocryst at the edge of a fragment of brecciated tuff has an overgrowth of An_{10} composition that extends into the hydrothermal cement. Small euhedral albite crystals in the youngest hydrothermal cement of the B-3 breccia are An_0 in composition.

Iron-rich epidote was found in minor amounts only in well B. Relationships among titanite, allanite, and epidote suggest that the titanite formed first and the epidote last (Fig. 6D). In those occurrences, the titanite forms clear, brownish, lumpy or spongy-looking crystals with the allanite blades scattered around them. Several allanite crystals are intergrown with the outer parts of the titanite crystals, and the epidote, in turn, rims the allanite (Fig. 6D). A few epidote-rimmed allanite crystals also grow into the pore spaces of adularia-lined fractures. Chlorite is the principal phyllosilicate mineral throughout well B, occurring as a fracture-filling mineral with calcite at shallower levels and with adularia at deeper levels. Chlorite also is the dominant replacement mineral of biotite and amphibole phenocrysts. K-mica has crystallized in small-scale fractures of B-1 and B-2, but at deeper levels it usually is confined to specific clasts. Some small, hydrothermal iron oxides occur as rod-shaped inclusions in quartz, but only scattered occurrences of the TiO_2 mineral—generally rimmed by titanite—were found. Small zircon crystals appear as inclusions in vein quartz.

Relative Fracture Orientations

As the core samples from these wells were not oriented, it is not possible to determine unambiguously the absolute orientation of structural features observed in the core. Rather, orientations of fractures and other deformation features on the core surfaces and in the thin sections were measured relative to a reference 0° azimuth line drawn down the length of each sample (see Moore, 1997, for details). Because this 0° line was arbitrarily selected for each piece of core, it does not represent
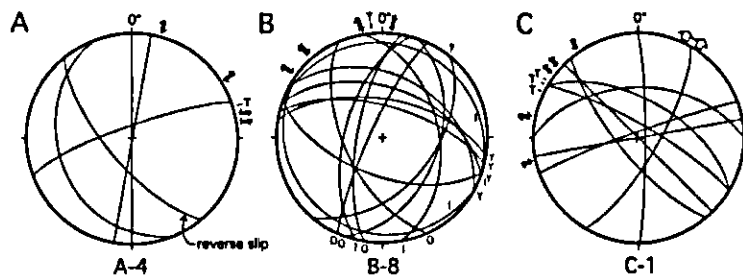
Figure 7. Combined microstructural data from three representative core samples as labeled, plotted on lower-hemisphere, equal-area stereonets. Orientations in a given core sample were made relative to an arbitrary 0° reference line drawn down the length of the core surface (see text for further explanation) and does not represent the true orientation of the sample (see Fig. 12). Great circles are macroscopic fractures observed on the core samples, and the longitudinal axis of each core lies at the center of the corresponding stereonet. Relative ages of the macroscopic fractures in B-8 are based on crosscutting relationships: Y—young; I—intermediate; O—old;? —probably old, but no conclusive evidence. Offset arrows are placed at the strikes of microfractures showing displacement in thin section; T labels are placed at the strikes of obvious tensile microcracks. All of the measured microstructures are associated with hydrothermal features, and they are not artifacts of the drilling process.

either the true orientation of a given sample or equivalent orientations in different samples. The structural data were plotted on lower-hemisphere, equal-area stereonets (Moore, 1997); an example from each well is presented in Figure 7. Strike and dip measurements were made only for those macroscopic fractures that could be traced around the perimeter of a piece of core; these data are plotted as great circles. The relative ages of most of the numerous macroscopic fractures in B-8 (Fig. 7B) could be estimated on the basis of crosscutting relationships.

Although several of the macroscopic fractures have a sheared appearance characterized by smeared-out, fine-grained rock, displacements could be measured only along three steeply dipping fractures for which offset lithic fragments indicate ~1 cm reverse slip (e.g., Fig. 7A). Throughout wells A and C, steeply dipping zones of alteration with subhorizontal slickensides were encountered (R. Hickman, 1997, 2000, personal communication) that were interpreted to be the damage zones associated with minor faulting. We presume that most of the nearly vertical shears in our samples also moved horizontally, mimicking the strike-slip motion of the Great Sumatran fault zone. However, horizontal offsets are much more difficult to identify on the core surfaces than vertical offsets, because of the smaller amount of exposed cross-sectional area.

In contrast, a number of microscopic fractures are offset by as much as 0.75 mm in either a right- or left-lateral direction. Only the

strikes of these microfaults were determined, although typically they appear to have near-vertical orientations in thin section; these strike measurements are plotted as paired offset arrows around the perimeter of each stereonet (Fig. 7). Several tensile microcracks were also identified. The strikes of those tensile cracks whose walls moved directly apart are designated by the letter T. The walls of a few tensile cracks separated obliquely, and the opening directions of such crack walls are marked by outward-pointing arrows. In each of the three wells, the microfractures with right-lateral offsets have strikes that fall within a relatively broad range of 20°–40° (Fig. 7), and those with left-lateral offsets form a second, more tightly clustered group oriented ~20°–30° clockwise from the closest right-slip microfracture. Tensile cracks have orientations between those of the right- and left-offset fractures.

DISCUSSION

Controls on Hydrothermal Assemblages

The dominant controls on the formation of hydrothermal mineral assemblages are usually temperature, fluid composition, and permeability (Browne, 1978) combined with fluid-rock ratio, and these factors are all important in the Silangkitang geothermal field. Mineralogical and textural observations from the Silangkitang core samples are evaluated in the Discussion in order to set limits on these key

parameters within the geothermal system and to determine changes with time.

Temperature Controls

Temperatures within a geothermal system can be established through the characterization of mineral assemblages and the evaluation of temperature-dependent variations in mineral composition. The relationship between temperature and mineral assemblage in the Silangkitang geothermal field is illustrated by comparison to the Salton Sea geothermal field, California (Fig. 8) (Muffler and White, 1969), which is developed in sedimentary deposits at the northern end of the Gulf of California. There, illite-montmorillonite is completely converted to well-crystallized K-mica at a temperature of ~210 °C. K-mica is abundant to ~290–300 °C, but its occurrence is uneven at higher temperatures (see also McDowell and Elders, 1980). Calcite is very common throughout the shallower parts of the sections, but it too disappears at temperatures above ~290–310 °C. In contrast, chlorite first appears at temperatures between 120 and 200 °C and becomes progressively more abundant with increasing depth and temperature to the roughly 320 °C maximum temperature encountered in the Salton Sea wells. Iron-rich epidote first appears and hydrothermal K-feldspar becomes abundant at temperatures near 290 °C. As can be seen from a comparison of Figure 8 with Table 1, the well C Silangkitang sample corresponds to the ~200 °C conditions in the Salton Sea wells, where K-mica and calcite are common and chlorite is scarce. Similarly, the well A assemblages are consistent with the temperature interval just below the first occurrence of epidote, characterized by abundant K-mica, chlorite, and calcite, whereas well B corresponds to the higher-temperature adularia + chlorite + epidote-bearing Salton Sea assemblages.

Variations in the compositions of K-mica and chlorite among the three wells (Moore, 1997) are also consistent with these temperature differences. The basic muscovite formula, $K_2Al_4(Si_6Al_2)O_{20}(OH)_4$, can be modified through a series of substitutions. The Silangkitang K-micas have moderate substitutions, principally of illite and phengite type, where the illite exchange is $K^{IV}Al = \square Si$ and the phengite exchange is $^{VI}Al^{IV}Al = (Mg,Fe^{2+})Si$. Overall, the well C micas have the largest illite-type substitutions, which is consistent with the lower well C temperatures. Substitution of Al^{3+} for Si^{4+} in the tetrahedral site of chlorite, $(Mg,Al,Fe)_{12}[(Si,Al)_8O_{20}](OH)_{16}$, is balanced by substitution of Al^{3+} for $(Mg,Fe)^{2+}$ in the octahedral sites. However, ^{VI}Al exceeds
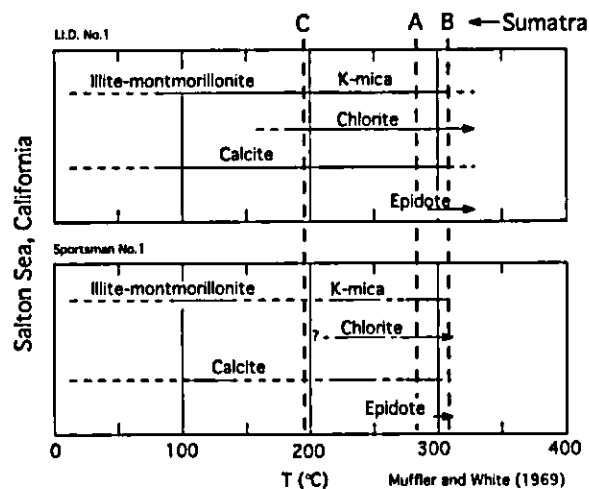
Figure 8. Summary of key mineral changes with increasing temperature in two wells from the Salton Sea geothermal field, modified from Figure 8 of Muffler and White (1969, p. 175). Arrows show minerals abundant at least to the maximum temperature encountered in a given well. The mineral assemblages and reported temperatures (mean values shown as vertical dashed lines) for the examined core samples from wells A, B, and C are consistent with the Salton Sea assemblages.

Figure 9. Chlorite compositions. (A) ^{IV}Al vs. ^{VI}Al, showing a modest direct relationship between the two. The ^{VI}Al contents are consistently in excess of ^{IV}Al. (B) Plot of ($^{VI}Al - ^{IV}Al$) relative to octahedral site occupancy, where the total number of octahedral sites is 12.0. The diagonal line represents the ideal exchange reaction of two ^{VI}Al ions plus one $^{[VI]}$ for three divalent cations, as suggested by Foster (1962). Small concentrations of monovalent cations in the chlorite analyses shift several of the points above the line. Data are from Moore (1997).

the ^{IV}Al content of all the Silangkitang chlorites (Fig. 9A). Foster (1962) suggested that excess ^{VI}Al is balanced by vacancies in the octahedral sites, according to the reaction $3(Mg,Fe^{2+}) = 2Al^{3+} + \square$. This exchange reaction creates one crystallographic vacancy for every two excess Al ions present and is consistent with the trends exhibited by the Silangkitang chlorites (Fig. 9B). McDowell and Elders (1980) found that the number of octahedral vacancies in chlorites from the Salton Sea geothermal field decreased with increasing temperature. We see the same trend in the Silangkitang chlorites: the two analyzed crystals from lower-temperature well C have some of the largest numbers of vacancies, whereas the smallest numbers of vacancies and excess ^{VI}Al ions are found in well B chlorites (Fig. 9).

Permeability Controls

The relative permeability of core samples from a geothermal system can be characterized by mineral indicators, degree of alteration, and textural features such as the presence of euhedral crystals growing into open fractures and veins, secondary porosity, and brecciation. Browne (1970) correlated the relative permeability of wells at Ohaaki-Broadlands, New Zealand, with their feldspar mineral assemblage, such that with progressively increasing permeability the mineral sequence is (1) primary andesine, (2) albite, (3) albite + adularia, and (4) adularia. This sequence was developed in rhyolitic ash-fall and ash-

flow tuffs similar to the Silangkitang core samples. If we use this classification scheme, well B would correspond to stages 3 to 4 (i.e., the highest relative permeability), well C to stages 2 to 3, and well A to stages 1 to 2. The igneous textures observable in thin section do not indicate any marked differences in primary rock porosity among the tuff samples we studied; instead, the feldspar contents are correlated with the development of secondary porosity. For example, well B is associated with the largest amount of secondary, connected pore space, resulting from extensive fracturing and the development of the brecciated zones. In contrast, the well A samples contain no open, dilational fractures lined with euhedral minerals of the sort common in wells B and C (e.g., Fig. 5A).

We can also use feldspar assemblages to distinguish between diffuse and channelized flow and to identify differences in cumulative water/rock ratio (Henneberger and Browne, 1988) among the wells. On the basis of the extensive hydrothermal cementation, the well B samples have been subject to by far the largest amount of pervasive hydrothermal fluid flow, even though fluid flow now appears to be concentrated in the open fractures and fluid-rock interaction currently is largely limited to the fracture walls and the breccia fragments. Rapid development of channelized flow may account for the partial preservation of the well B igneous feldspar compositions. Although the well C sample contains some open fractures and microfractures, the perva-
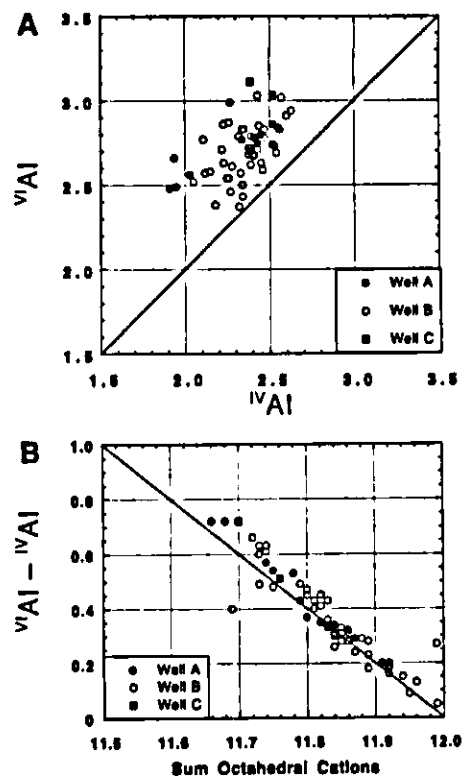
sive alteration of the feldspar phenocrysts is evidence for significant diffusive flow through the tuff. The good preservation of relict sanidine and andesine phenocryst compositions—including many ground-up phenocrysts in the sheared bands—suggests that the fluid/rock ratio for well A has been significantly lower than for the other wells.

Fluid Compositional Controls

The composition of geothermal fluids can be determined by the presence, absence, or coexistence of mineral phases. The presence of calcite instead of a Ca-zeolite in the ~200 °C well C core sample and the restricted occurrence of epidote among the higher-temperature core samples are significant in this regard. In New Zealand, the Wairakei geothermal field is

characterized by abundant wairakite and epidote but little calcite, whereas the nearby Ohaaki-Broadlands field has abundant calcite and only minor epidote and wairakite at comparable temperatures and in similar rhyolitic tuffs (Browne and Ellis, 1970). Browne and Ellis (1970) attributed the differences in mineral assemblage to the much higher P_{CO_2} and low Ca contents of the hydrothermal fluids at Ohaaki-Broadlands compared to Wairakei. Thus, the absence of Ca-zeolites as well as the scarcity of epidote may be a function of high P_{CO_2} ± low Ca concentrations. Muffler and White (1969) also attributed the lack of zeolites in the Salton Sea wells that they examined to high CO_2 activity relative to that of H_2O at shallow depths, resulting from decarbonation reactions. Unpublished data obtained by Unocal from flow tests of well B (R. Gunderson, 2000, personal communication) indicate that the CO_2 contents of the reservoir fluid are comparable to or slightly higher than those reported by Giggenbach (1995) for the CO_2-rich fluid compositions encountered at the Broadlands, Kawerau, and Rotokawa geothermal fields in the Taupo Volcanic Zone of New Zealand.

Pyrite and hematite coexist in the Salton Sea wells, which suggests that oxygen fugacities are in the range 10^{-26} to 10^{-28} MPa and sulfur fugacities are in the range $10^{-6.7}$ to $10^{-8.3}$ MPa at a temperature of ~325 °C (Muffler and White, 1969). Well B contains pyrite and either hematite or magnetite at nearly this same temperature and should therefore reflect comparable oxygen and sulfur fugacities. The near absence of pyrite in well A indicates that these fluids have relatively lower sulfur fugacities than those of well B, but the late-crystallized pyrite suggests a recent change. In the ~200 °C well C sample, igneous magnetite is being resorbed and pyrite has crystallized, which suggests a minimum sulfur fugacity of ~10^{-15} MPa (Liou et al., 1985).

Temporal Changes

The presence of crosscutting veins, mineral overgrowths and resorption features, and differing mineral assemblages and compositions can be used to track changes in temperature, fluid chemistry, and/or permeability with time. Because of the larger number of well B samples available for study, an approximate time sequence of hydrothermal mineral growth and relative mineral abundances could be constructed for that well (Fig. 10). The transition from K-mica + calcite to adularia + chlorite + epidote assemblages in Figure 10 roughly follows the temperature sequence of Figure 8, which suggests the possibility of increasing

temperature over time. The increasing Ca content of albite (Figs. 4 and 10) also is consistent with such a trend (e.g., Cho et al., 1988). Changing fluid chemistry may play a role, particularly with respect to the stability of calcite versus that of epidote. The onset of allanite crystallization reflects the attainment of sufficiently high rare earth element concentrations for its growth, because allanite is the principal sink for rare earth elements in these rocks.

The breccia zones of well B may develop through progressive, episodic opening along networks of intersecting cracks, with concomitant increases in their permeability. Such increases might be marked by enhanced deposition of adularia-rich cement, perhaps during episodes of boiling (Browne and Ellis, 1970; White and Hedenquist, 1990). Browne and Ellis (1970) attributed the appearance of epidote at Ohaaki-Broadlands to loss of a few percent steam during boiling. In addition, the relatively late appearance of anhydrite may be correlated with the generation of extensive fracture permeability during faulting or fault-valve behavior (e.g., Sibson, 1992). Because the solubility of anhydrite decreases with decreasing pressure, it may precipitate in areas where pressure drops rapidly (Rimstidt, 1997), and the anhydrite in well B occurs preferentially in the larger open fractures and void-rich brecciated zones.

In well A, as noted previously, a recent change in fluid chemistry may have led to the crystallization of traces of pyrite and other sulfur-bearing minerals. Other, possibly temperature-related changes in well A samples include the increase in An content of hydro-

thermal plagioclase with time and the transition from K-mica + TiO_2 to chlorite + titanite assemblages after biotite with increasing depth and perhaps with time.

Fracture Types and Orientations within the Great Sumatran fault zone

Subsidiary shears with characteristic offset directions and orientations in simple-shear systems have been identified within natural and laboratory fault zones (Fig. 11) (e.g., Logan et al., 1979; see summary by Sylvester, 1988). In a series of rotary shear experiments employing photoelastic sensors, Mandl et al. (1977) demonstrated that in a simple-shear system, σ_1 is reoriented such that it makes a 45° angle to the shear direction at the time of peak stress. Tensile fractures (T) form parallel to σ_1, and the R, Y, and P traces all have the same sense of offset as the shear zone (Fig. 11). Y traces are nearly parallel to the overall strike of the fault zone, whereas R and P traces make small to moderate angles of opposite sign relative to the strike of the fault zone. The R and R′ traces are generally equated with Coulomb shears (Hansen, 1961; Morgenstern and Tchalenko, 1967; Tchalenko, 1970). During laboratory faulting experiments, the R traces typically form first, followed by P and then Y traces (e.g., Morgenstern and Tchalenko, 1967; Mandl et al., 1977). As discussed by Tchalenko (1970) and Wallace (1973), the internal features of a fault zone may be scale invariant, that is, the same geometry develops at scales ranging from millimeters to kilometers. For this discussion, we consider the Great Sumatran fault zone to span the 4–6-km-wide
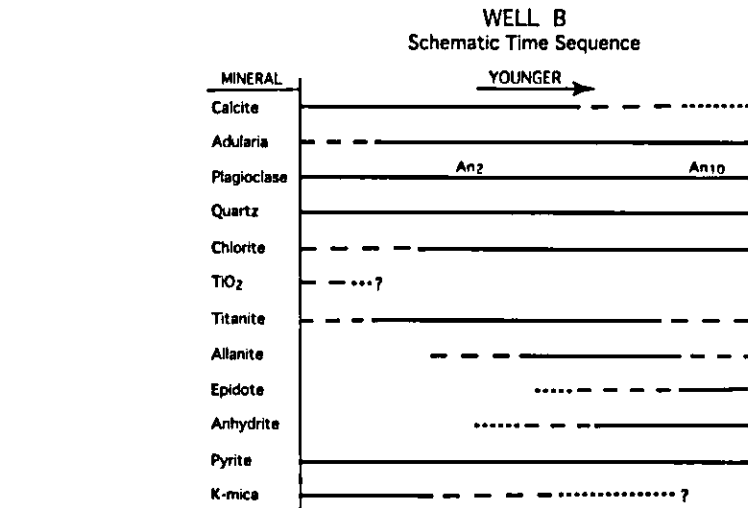

Figure 10. Schematic time sequence of hydrothermal mineral growth in well B, inferred from the textural and compositional data described in the text.
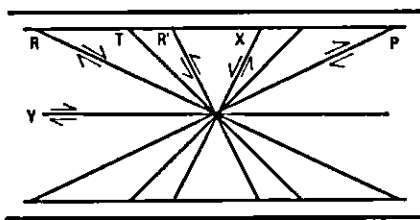
Figure 11. Letter-labeling scheme that is commonly used to refer to subsidiary fault traces with specific orientations and offset directions relative to the overall strike of the fault zone, adapted from Logan et al. (1979). The Y, R, and P traces are typically the most commonly observed traces in a given fault zone, and they have the same sense of displacement as the fault. The Y traces are subparallel to the strike of the fault zone, and both R and P traces typically are oriented at angles of <35°, but with opposite signs to the fault strike. Fractures labeled T are tensile cracks. The R and R' traces are considered to correspond to Coulomb shears. The X traces were added by Logan et al. (1979) principally for symmetry; such traces are rarely found in either natural or laboratory faults.
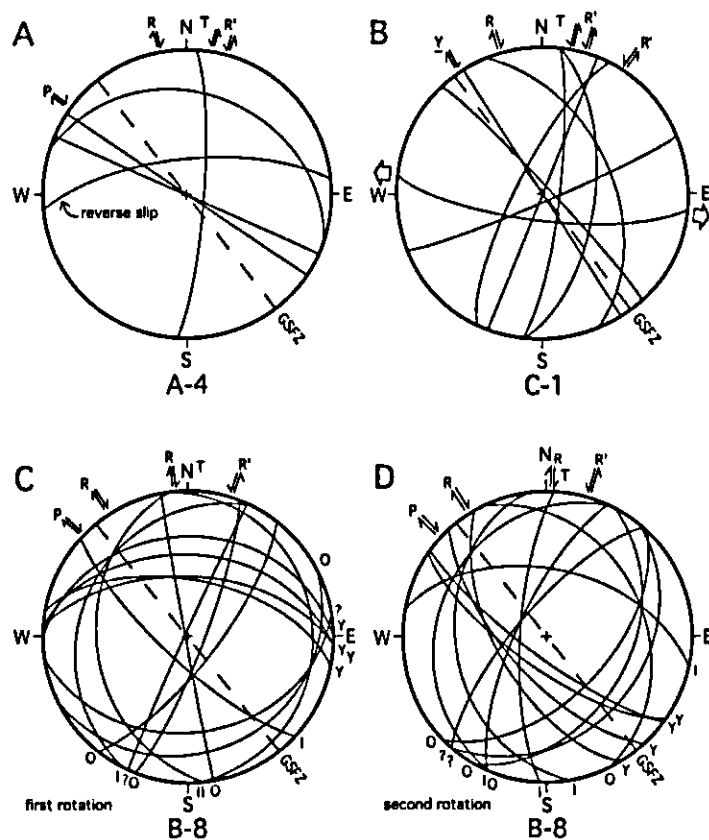

Figure 12. Microstructural data from Figure 7 reoriented such that the tensile microcracks (T) are at 45° to the strike of the Great Sumatran fault zone (GFSZ), shown as a dashed line. Letter labels are assigned to the offset arrows according to the scheme in Figure 11. Samples: (A) A-4; (B) C-1; (C) and (D) attempts to restore the stereonet for B-8 (core from the deviated well) to its possible original orientation (see text). For C, the stereonet was first rotated 12° clockwise, followed by a second rotation to make the core dip 60° in the direction S84°E. In D, the initial rotation was 82° + 180° clockwise, and then the core was rotated to a 60° dip. The relative ages of the macroscopic fractures in B-8 are noted in the same way as in Figure 7.

zone between the western and eastern fault strands (Fig. 2B) and all three wells to be affected by the stress fields within the fault zone. This assumption is consistent with recent reports of a rotation of the maximum horizontal stress associated with the San Andreas fault in central and southern California from ~60°–90° to the strike of the fault in the far field to ~40°–50° in a zone a few kilometers wide centered on the fault (e.g., Provost and Houston, 1999; Hardebeck and Hanksson, 1999).

From comparison with Figure 11, the left-slip fractures in Figure 7 may correspond to R' traces, and the right-slip ones, with their wider range of orientations, to R, Y, or P traces. This correspondence suggests that potentially the core samples can be oriented relative to the strike of the Great Sumatran fault zone, according to the relationships in Figure 11. The process is illustrated in Figure 12, A and B, for the A-4 and C-1 stereonets of Figure 7, respectively; an average strike of N38°W for the fault zone near Silangkitang was assumed, and each stereonet was rotated about a vertical axis until the tensile microcracks made a 45° angle to the strike of the fault. The arrangement of shear planes in Figure 11 looks the same when the figure is rotated 180°; thus, two possible matches exist for each piece of core, the one illustrated and the second at 180°

rotation to the first. For A-4 and C-1, which come from wells that were drilled nearly vertically, the 180° rotation only affects the direction of dip of the macroscopic fractures, which are plotted as great circles on the stereonets. In the absence of borehole image data from these wells against which to compare our relative fracture orientations, three-dimensional information on the microfault orientations or paleomagnetic measurements might aid in the identification of a single preferred orientation for a given core sample, but such an analysis is beyond the scope of this study.

An additional step is required in the attempt to orient the well B samples, because the original fracture measurements assumed a vertical core axis, whereas well B is inclined at ~60° in the direction S84°E. To produce Figure 12C from Figure 7B, the stereonet first was aligned roughly consistent with the strike of the Great

Sumatran fault zone by rotating it 12° clockwise about a vertical axis. The stereonet was then rotated 30° counterclockwise about a horizontal axis trending N6°E, to account for the inclination of the well. For Figure 12D, the stereonet was first rotated 12° + 180° clockwise about the vertical axis and then 30° counterclockwise about the N6°E horizontal axis. In both cases, the second rotation about the horizontal axis shifted the strike of the tensile cracks by ≤1°.

Overall, the macroscopic fractures in Figure 12D dip more steeply than those in Figure 12C, making Figure 12D more consistent with the fracture patterns of the well A and well B examples (Fig. 12, A and B). Moreover, the four relatively young macroscopic fractures in Figure 12C not only are relatively shallow dipping (30°–60°), but they are also oriented at large angles to the strike of the Great Su-

matran fault zone. In contrast, those same four fractures in Figure 12D have dips of 60°–80°, and their strikes are similar to that of the fault zone. The second case (Fig. 12D) may therefore be the more reasonable choice of the two. One additional feature of Figure 12D is that, with a couple of exceptions, the strikes of the macroscopic fractures shift in a counterclockwise direction from oldest to youngest. The significance of such a trend is not clear at this time.

In laboratory shearing experiments, which typically are conducted at elevated confining pressures, R' and P traces are relatively uncommon features (e.g., Moore and Byerlee, 1991, 1992), and Vialon (1979) and Gamond (1983) have suggested that the development of P and R' traces is suppressed in fault zones where dilation is inhibited. As illustrated by the arrangement of offset arrows in Figure 12, the microcracks with measurable offsets include several left-lateral R' traces as well as some right-lateral traces whose orientations correspond most closely to P traces. This finding is consistent with the location of the wells within the extensional environment of the Sarulla graben (Gunderson et al., 2000).

The Hydrothermal System and the Great Sumatran Fault Zone

Figure 13 illustrates the possible relationships between wells A and B in a schematic, east-west cross section (section line shown in Fig. 2B). The fluid reservoir for the Silangkitang geothermal field has an elongate form, underlying the 1 km × 4 km band of surface geothermal features that follows the main trace of the Great Sumatran fault zone (Fig. 2B). The well B core samples, therefore, may lie directly above the reservoir, and their high secondary permeability, which provides a conduit for the geothermal fluids, can be explained by their position within the fault zone. Exhumed strike-slip fault zones in crystalline rocks tend to be characterized by a narrow, gouge-bearing core surrounded by a wide damage zone of fractured country rock (e.g., Chester and Logan, 1986; Chester et al., 1993). Within the damage zone, fractures are reopened or new ones created during succeeding earthquakes. Lockner et al. (2000) measured the permeability of core samples from the Nojima fault zone of Japan, which ruptured during the 1995 Kobe earthquake. They found that the matrix permeability of granodiorite from the damage zone, which contained abundant grain-scale microcracks, is four to five orders of magnitude higher than that of the country rock. Interaction between
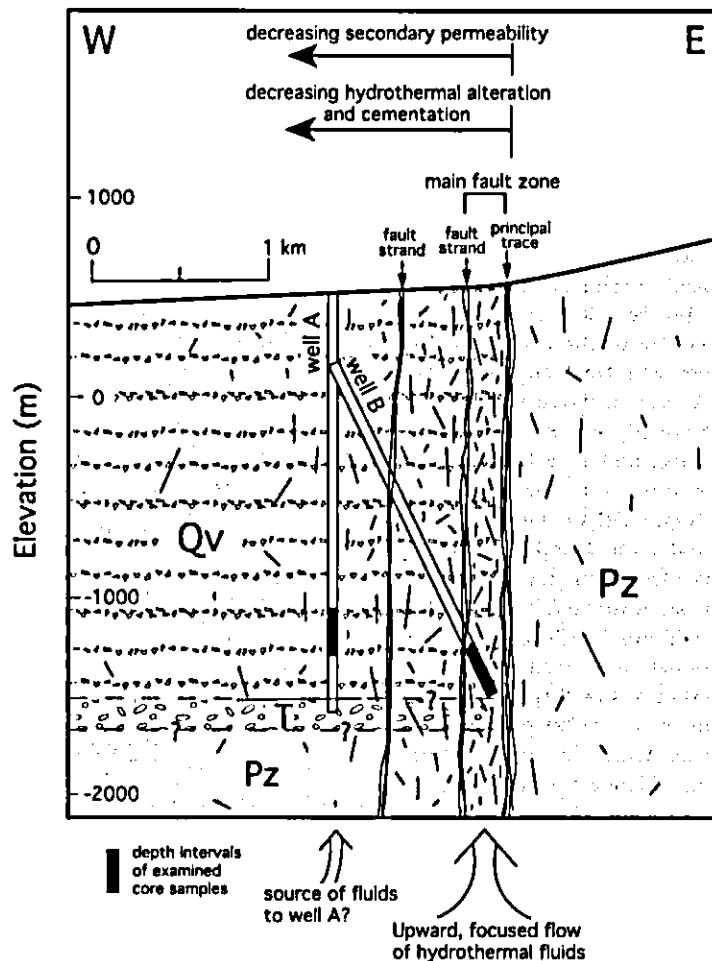

Figure 13. Schematic, east-west cross section near wells A and B (section line shown in Fig. 2B). Two subsidiary fault strands crossed during the drilling of well B are situated between well A and the principal trace; the more easterly strand is interpreted to be the one encountered ~40 m west of sample B-1. Tertiary (T) sedimentary rocks were encountered in the lowermost 100 m of well A, and the Paleozoic (Pz) sequence may begin ~100 m below well A. Arrows at the top show secondary permeability and the intensity of hydrothermal overprint decreasing westward from the principal trace; stepwise changes may occur at the two fault strands. Ascent of hot, hydrothermal fluids from a large reservoir is focused between the eastern subsidiary trace and the principal fault trace (see Gunderson et al., 1995, 2000). The intensity of fracturing (indicated by the concentration of short, solid lines) appears to diminish away from this primary fault zone and could in part account for the lower amount of water-rock interaction observed in well A.

the principal fault trace and the subsidiary fault strand immediately west of it may further enhance the permeability of the examined well B samples (e.g., Curewitz and Karson, 1997).

Given their positions farther from the principal trace, the well A and well C core samples would be expected to have permeability closer to that of the country rock than those from well B, which is in general agreement with the petrographic observations. The well C drilling site is closer to a mapped subsidiary fault trace than the well A site, which may explain its slightly higher inferred fracture

permeability. On the basis of its hydrothermal mineral assemblage, the well C sample has interacted with fluids whose composition was similar to those present in well B but to a lesser extent and at a lower temperature. If wells B and C do receive fluids from the same reservoir, a smaller amount of fluid that largely moves in a diffusive manner through the primary rock porosity could account for the lower-temperature alteration of well C.

The somewhat distinctive alteration mineral assemblage of well A suggests that this part of the Silangkitang geothermal system may

CONCLUSIONS

Hydrothermal mineral assemblages vary among the core samples of tuff examined from three wells in the Silangkitang geothermal field along the Great Sumatran fault zone, re-flecting differences in temperature, fluid chemistry, secondary fracture permeability, and fluid/rock ratio. Fault-zone architecture and hydromechanical processes, in turn, are responsible for many of these observed dif-ferences. Indeed, the concentration of surface geothermal features in a narrow band along the principal trace of the fault zone indicates that the location of the geothermal reservoir itself is fault controlled. The permeability of the core samples correlates with their posi-tions relative to the principal trace of the fault zone, suggesting that high fault-zone perme-abilities are maintained by fracturing and fault reactivation within the damage zone, perhaps augmented by extensional strains induced by interaction between the principal trace and an adjacent, subsidiary fault strand. In particular, the highest-permeability samples come from well B, drilled closest to the principal trace, and they are characterized by the presence of hydrothermal breccias and associated chan-nelized flow, high fluid/rock ratios, and the highest-temperature alteration assemblages. The other two wells (A and C) have lower permeability and are sited along the south-western edge of the zone of subsidiary fault-ing associated with the principal trace. The

have a different or modified fluid source com-pared to that of the other two wells, along with a lower fluid/rock ratio. Because of the limited available data, we can only speculate about the cause. A contrast in bulk host-rock per-meability between well A and the main up-flow area along the principal trace of the Great Sumatran fault zone (Fig. 13) is one possible mechanism. However, the pervasive alteration of the well C sample suggests that hydrother-mal fluid migration occurs relatively uniform-ly within the Quaternary volcanic rock section in the Sarulla graben. Alternatively, one of the subsidiary fault strands identified during dril-ling of well B (Fig. 13) could serve as a per-meability barrier. In this regard, the perme-ability of the fine-grained gouge from the Nojima fault zone is substantially lower than that of the damage zone (Lockner et al., 2000). In general, the fabric of fault gouge can cause permeability to be significantly lower perpen-dicular to the fault plane than parallel to it (e.g., Knipe, 1992, 1993; Evans et al., 1997); thus, fault gouge, if present, would restrict flu-id flow across the fault.

core sample from well C shows evidence of diffuse flow of a relatively low-temperature fluid and moderate fluid/rock ratios, consistent with slower flow over a longer, perhaps more tortuous path from the main reservoir. Well A not only has low permeability but also the lowest fluid/rock ratios; the alteration assem-blages from well A indicate a somewhat dif-ferent fluid chemistry from that of the other wells. Overall, these features suggest that flow of hot, hydrothermal fluids at this locality has been focused in a narrow zone around the principal trace of the Great Sumatran fault zone and that a secondary fault strand may act as a permeability barrier between the main reservoir and well A. The absence of zeolites from the lowest-temperature core sample, the general abundance of calcite, and the scarcity of epidote are consistent with relatively high P_{CO_2} of the hydrothermal fluids, suggesting a magmatic source for the gases.

REFERENCES CITED

Aspden, J.A., Kartawa, W., Aldiss, D.T., Djunuddin, A., Whandoyo, R., Diatma, W., Clarke, M.C.G., and Har-ahap, H., 1982, The geology of the Padangsidempuan and Sibolga Quadrangle, Sumatra: Bandung, Indone-sia, Directorate General of Mines, Geological Re-search and Development Center, scale 1:250 000.
Bellier, O., and Sébrier, M., 1994, Relationship between tectonism and volcanism along the Great Sumatran fault zone deduced by SPOT image analysis: Tecton-ophysics, v. 233, p. 215–231.
Bellier, O., and Sébrier, M., 1995, Is the slip rate variation on the Great Sumatran fault accommodated by fore-arc stretching?: Geophysical Research Letters, v. 22, p. 1969–1972.
Browne, P.R.L., 1970, Hydrothermal alteration as an aid in investigating geothermal fields: Geothermics Special Issue, v. 2, p. 564–570.
Browne, P.R.L., 1978, Hydrothermal alteration in active geothermal fields: Annual Review of Earth and Plan-etary Sciences, v. 6, p. 229–250.
Browne, P.R.L., and Ellis, A.J., 1970, The Ohaki-Broad-lands hydrothermal area, New Zealand: Mineralogy and related geochemistry: American Journal of Sci-ence, v. 269, p. 97–131.
Chester, F.M., and Logan, J.M., 1986, Implications for me-chanical properties of brittle faults from observations of the Punchbowl fault zone, California, in Wang, C.-Y., ed., Internal structure of fault zones: Pure and Ap-plied Geophysics, v. 124, p. 79–106.
Chester, F.M., Evans, J.P., and Biegel, R.L., 1993, Internal structure and weakening mechanisms of the San An-dreas fault: Journal of Geophysical Research, v. 98, p. 771–786.
Cho, M., Liou, J.G., and Bird, D.K., 1988, Prograde phase relations in the State 2–14 well metasandstones, Sal-ton Sea geothermal field, California: Journal of Geo-physical Research, v. 93, p. 13081–13103.
Curewitz, D., and Karson, J.A., 1997, Structural settings of hydrothermal outflow: Fracture permeability main-tained by fault propagation and interaction: Journal of Volcanology and Geothermal Research, v. 79, p. 149–168.
Evans, J.P., Forster, C.B., and Goddard, J.V., 1997, Per-meability of fault-related rocks, and implications for hydraulic structure of fault zones: Journal of Structural Geology, v. 19, p. 1393–1404.
Fauzi, McCaffrey, R., Wark, D., Sunaryo, and Prih Hary-adi, P.Y., 1996, Lateral variation in slab orientation beneath Toba caldera, northern Sumatra: Geophysical Research Letters, v. 23, p. 443–446.
Fitch, T.J., 1972, Plate convergence, transcurrent faults and internal deformation adjacent to southeast Asia and the western Pacific: Journal of Geophysical Research, v. 77, p. 4432–4460.
Foster, M.D., 1962, Interpretation of the composition and a classification of the chlorites: U.S. Geological Survey Professional Paper 414-A, 33 p.
Gamond, J.F., 1983, Displacement features associated with fault zones: A comparison between observed exam-ples and experimental models: Journal of Structural Geology, v. 5, p. 33–45.
Giggenbach, W.F., 1995, Composition of fluids in geother-mal systems of the Taupo Volcanic Zone, New Zea-land, as a function of source magma, in Kharaka, Y.K., and Chudaev, O.V., eds., Water-Rock Interac-tion, Proceedings of the 8th International Symposium on Water-Rock Interaction: Brookfield, Vermont, A.A. Balkema Publishers, p. 9–12.
Gunderson, R.P., Dobson, P.F., Sharp, W.D., Pudjianto, R., and Hasibuan, A., 1995, Geology and thermal features of the Sarulla contract area, North Sumatra, Indonesia: World Geothermal Congress, Proceedings, v. 2, p. 687–692.
Gunderson, R., Ganefianto, N., Riedel, K., Sirad-Azwar, L., and Suleiman, S., 2000, Exploration results in the Sa-rulla block, North Sumatra, Indonesia: World Geo-thermal Congress 2000, Proceedings, p. 1183–1188.
Hamilton, W., 1979, Tectonics of the Indonesian region: U.S. Geological Survey Professional Paper 1078, p. 18–38.
Hansen, B., 1961, Shear box tests on sand: 5th International Conference on Soil Mechanics, Proceedings: Paris, France, Dunod, v. 1, p. 127–131.
Handcheck, J.L., and Hankssson, E., 1999, Role of fluids in faulting inferred from stress field signatures: Science, v. 285, p. 236–239.
Hennebergir, R.C., and Browne, P.R.L., 1988, Hydrother-mal alteration and evolution of the Ohakuri hydro-thermal system, Taupo Volcanic Zone, New Zealand: Journal of Volcanology and Geothermal Research, v. 34, p. 211–231.
Hickman, S.H., 1991, Stress in the lithosphere and the strength of active faults, U.S. National Report to In-ternational Union of Geodesy and Geophysics 1987–1990: Reviews of Geophysics, v. 29, p. 759–775.
Hickman, S., Sibson, R., and Bruhn, R., 1995, Introduction to special section: Mechanical involvement of fluids in faulting: Journal of Geophysical Research, v. 100, p. 12831–12840.
Hochstein, M.P., and Sudarman, S., 1993, Geothermal re-sources of Sumatra: Geothermics, v. 22, p. 181–200.
Katili, J.A., 1970, Large transcurrent faults in Southeast Asia, with special reference to Indonesia: Geologische Rundschau, v. 59, p. 581–600.
Knipe, R.J., 1992, Faulting processes and fault seal, in Lar-sen, R.M., et al., eds., Structural and tectonic model-ling and its application to petroleum geology: Nor-wegian Petroleum Society Special Publication, v. 1, p. 325–342.
Knipe, R.J., 1993, The influence of fault zone processes and diagenesis on fluid flow, in Horbury, A.D., and Robinson, A.G., eds., Diagenesis and basin develop-ment: American Association of Petroleum Geologists Studies in Geology 36, p. 135–151.
Liou, J.G., Seki, Y., Guillemette, R.N., and Sakai, H., 1985, Compositions and parageneses of secondary minerals in the Onikobe geothermal system, Japan: Chemical Geology, v. 49, p. 1–20.
Lockner, D., Naka, H., Tanaka, H., Ito, H., and Ikeda, R., 2000, Permeability and strength of core samples from

the Nojima fault of the 1995 Kobe earthquake, *in* Ito, H., et al., eds., Proceedings of the International Workshop on the Nojima fault core and borehole data analysis: U.S. Geological Survey Open-File Report 00-129, p. 147–152.

Logan, J.M., Friedman, M., Higgs, N., Dengo, C., and Shimamoto, T., 1979, Experimental studies of simulated gouge and their application to studies of natural fault zones, *in* Proceedings of Conference VIII, Analysis of actual fault zones in bedrock: U.S. Geological Survey Open-File Report 79–1239, p. 305–343.

Mandl, G., de Jong, L.N.J., and Maltha, A., 1977, Shear zones in granular material: An experimental study of their structure and mechanical genesis: Rock Mechanics, v. 9, p. 95–144.

McCaffrey, R., 1996, Slip partitioning at convergent plate boundaries of SE Asia, *in* Hall, R., and Blundell, D., eds., Tectonic evolution of Southeast Asia: Geological Society [London] Special Publication 106, p. 3–18.

McCourt, W.J., Crow, M.J., Cobbing, E.J., and Amin, T.C., 1996, Mesozoic and Cenozoic plutonic evolution of SE Asia: Evidence from Sumatra, Indonesia, *in* Hall, R., and Blundell, D., eds., Tectonic evolution of Southeast Asia: Geological Society [London] Special Publication 106, p. 321–335.

McDowell, S.D., and Elders, W.A., 1980, Authigenic layer silicate minerals in borehole Elmore 1, Salton Sea geothermal field, California, USA: Contributions to Mineralogy and Petrology, v. 74, p. 293–310.

Moore, D.E., 1997, Mineralogical and microstructural investigations of core samples from the vicinity of the Great Sumatran fault, Indonesia: U.S. Geological Survey Open-File Report 97–694, 112 p.

Moore, D.E., and Byerlee, J., 1991, Comparative geometry of the San Andreas fault, California, and laboratory fault zones: Geological Society of America Bulletin, v. 103, p. 762–774.

Moore, D.E., and Byerlee, J., 1992, Relationships between sliding behavior and internal geometry of laboratory fault zones and some creeping and locked strike-slip faults of California: Tectonophysics, v. 211, p. 305–316.

Morgenstern, M.R., and Tchalenko, J.S., 1967, Microscopic structures in kaolin subjected to direct shear: Géotechnique, v. 17, p. 309–328.

Mount, V.S., and Suppe, J., 1987, State of stress near the San Andreas fault: Implications for wrench tectonics: Geology, v. 15, p. 1143–1146.

Mount, V.S., and Suppe, J., 1992, Present-day stress orientations adjacent to active strike-slip faults: California and Sumatra: Journal of Geophysical Research, v. 97, p. 11995–12013.

Muffler, L.J.P., and White, D.E., 1969, Active metamorphism of upper Cenozoic sediments in the Salton Sea geothermal field and the Salton trough, southeastern California: Geological Society of America Bulletin, v. 80, p. 157–182.

Newcomb, K.R., and McCann, W.R., 1987, Seismic history and seismotectonics of the Sunda arc: Journal of Geophysical Research, v. 92, p. 421–439.

Provost, A.-S., and Houston, H., 1999, Rotation in the stress field near the creeping zone of the San Andreas fault [abs.]: Eos (Transactions, American Geophysical Union), v. 80, p. F702.

Ramsay, J.G., 1980, The crack-seal mechanism of rock deformation: Nature, v. 284, p. 135–139.

Rimstidt, J.D., 1997, Gangue mineral transport and deposition, *in* Barnes, H.L., ed., Geochemistry of hydrothermal ore deposits (3rd edition): New York, John Wiley and Sons, p. 487–515.

Schulz, S.E., and Evans, J.P., 1998, Spatial variability in microscopic deformation and composition of the Punchbowl fault, southern California: Implications for mechanisms, fluid-rock interaction, and fault morphology, *in* Chester, F.M., et al., eds., Rock deformation: The Logan Volume: Tectonophysics, v. 295, p. 223–244.

Sibson, R.H., 1992, Implications of fault-valve behavior for rupture nucleation and recurrence: Tectonophysics, v. 211, p. 283–292.

Sieh, K., and Natawidjaja, D., 1998, The Great Sumatran fault, Indonesia [abs.]: Eos (Transactions, American Geophysical Union), v. 79, p. F888.

Sieh, K., and Natawidjaja, D., 2000, Neotectonics of the Sumatran fault, Indonesia: Journal of Geophysical Research, v. 105, p. 28295–28326.

Sieh, K., Zachariasen, J., Bock, Y., Edwards, L., Taylor, F., and Gans, P., 1994, Active tectonics of Sumatra: Geological Society of America Abstracts with Programs, v. 26, no. 7, p. A382.

Simandjuntak, T.O., and Barber, A.J., 1996, Contrasting tectonic styles in the Neogene orogenic belts of Indonesia, *in* Hall, R., and Blundell, D., eds., Tectonic evolution of Southeast Asia: Geological Society [London] Special Publication 106, p. 185–201.

Sylvester, A.G., 1988, Strike-slip faults: Geological Society of America Bulletin, v. 100, p. 1666–1703.

Tchalenko, J.S., 1970, Similarities between shear zones of different magnitude: Geological Society of America Bulletin, v. 81, p. 1625–1640.

Vialon, P., 1979, Les déformations continues–discontinues des roches anisotropes: Eclogae Geologicae Helvetiae, v. 72, p. 531–549.

Wallace, R.E., 1973, Surface fracture patterns along the San Andreas fault, *in* Kovach, R.L., and Nur, A., eds., Proceedings of the conference on tectonic problems of the San Andreas fault system: Stanford University Publications in Geological Science, v. 13, p. 248–250.

White, N.C., and Hedenquist, J.W., 1990, Epithermal environments and styles of mineralization: Variations and their cases, and guidelines for exploration: Journal of Geochemical Exploration, v. 36, p. 445–474.

Zoback, M.D., Zoback, M.L., Mount, V.S., Suppe, J., Eaton, J.P., Healy, J.H., Oppenheimer, D., Reasenberg, P., Jones, L., Raleigh, C.B., Wong, I.G., Scotti, O., and Wentworth, C., 1987, New evidence on the state of stress of the San Andreas fault system: Science, v. 238, p. 1105–1111.